

The Orion fingers: Near-IR adaptive optics imaging of an explosive protostellar outflow[★]

John Bally¹, Adam Ginsburg², Devin Silvia³, and Allison Youngblood¹

¹ Department of Astrophysical and Planetary Sciences, University of Colorado, UCB 389, Boulder, CO 80309, USA
e-mail: John.Bally@colorado.edu

² ESO Headquarters, Karl-Schwarzschild-Str. 2, 85748 Garching bei München, Germany

³ NSF Astronomy and Astrophysics Postdoctoral Fellow, Department of Physics and Astronomy, Michigan State University, East Lansing, MI 48824, USA

Received 28 September 2014 / Accepted 5 February 2015

ABSTRACT

Aims. Adaptive optics (AO) images are used to test the hypothesis that the explosive BN/KL outflow from the Orion OMC1 cloud core was powered by the dynamical decay of a non-hierarchical system of massive stars.

Methods. Narrow-band H₂, [Fe II], and broad-band K_s obtained with the Gemini South multi-conjugate AO system GeMS and near-IR imager GSAOI are presented. The images reach resolutions of 0.08 to 0.10'', close to the 0.07'' diffraction limit of the 8-m telescope at 2.12 μm. Comparison with previous AO-assisted observations of sub-fields and other ground-based observations enable measurements of proper motions and the investigation of morphological changes in H₂ and [Fe II] features with unprecedented precision. The images are compared with numerical simulations of compact, high-density clumps moving ~10³ times their own diameter through a lower density medium at Mach 10³.

Results. Several sub-arcsecond H₂ features and many [Fe II] “fingertips” on the projected outskirts of the flow show proper motions of ~300 km s⁻¹. High-velocity, sub-arcsecond H₂ knots (“bullets”) are seen as far as 140'' from their suspected ejection site. If these knots propagated through the dense Orion A cloud, their survival sets a lower bound on their densities of order 10⁷ cm⁻³, consistent with an origin within a few au of a massive star and accelerated by a final multi-body dynamic encounter that ejected the BN object and radio source I from OMC1 about 500 yr ago.

Conclusions. Over 120 high-velocity bow-shocks propagating in nearly all directions from the OMC1 cloud core provide evidence for an explosive origin for the BN/KL outflow triggered by the dynamic decay of a non-hierarchical system of massive stars. Such events may be linked to the origin of runaway, massive stars.

Key words. ISM: jets and outflows – ISM: clouds – stars: formation

1. Introduction

The BN/KL region behind the Orion Nebula, located at a distance of about 414 pc (Menten et al. 2007), contains a spectacular, wide opening-angle, arcminute-scale outflow emerging from the OMC1 cloud core. The flow is traced by the millimeter and sub-millimeter emission lines of molecules such as CO, CS, SO, SO₂, and HCN that exhibit broad (>100 km s⁻¹) emission line wings (Kwan & Scoville 1976; Wiseman & Ho 1996; Furuya & Shinnaga 2009), high-velocity OH, H₂O, and SiO maser emission (Genzel et al. 1981; Greenhill et al. 1998), and bright shock-excited “fingers” of H₂ and “fingertips” of 1.64 μm [Fe II] emission (Allen & Burton 1993; Colgan et al. 2007; Nissen et al. 2007; Lee & Burton 2000; Bally et al. 2011). The OMC1 outflow has a southeast (red-shifted) to northwest (blue-shifted) axis and contains at least 8 M_⊙ of accelerated gas with a median velocity of about 20 km s⁻¹. Interferometric CO images, H₂O and the 18 km s⁻¹ SiO masers, and dense-gas tracers such as thermal SiO emission reveal a smaller (8'' long) and younger (~200 yr old) outflow along a northeast-southwest axis emerging from radio source I orthogonal to the arc-minute-scale CO outflow (Beuther & Nissen 2008; Plambeck et al. 2009). The momentum and kinetic energy content of these flows is at least 160 M_⊙ km s⁻¹ and 4 × 10⁴⁶ erg (Snell et al. 1984) to

4 × 10⁴⁷ erg (Kwan & Scoville 1976). Zapata et al. (2009) presented a CO J = 2–1 interferometric study and found a dynamic age of about 500 yr for the larger OMC1 outflow. They noted that its impulsive nature and its structure is different from accretion-disk powered jets and collimated protostellar outflows, and that it originated several arcseconds north of the OMC1 hot-core.

Radio-frequency astrometry has shown that the three radio-emitting stars in OMC1, sources BN, I, and source n, have proper motions of 25, 13, and 26 km s⁻¹ away from a region less than 500 au in diameter from which they were ejected about 500 yr ago (Rodríguez et al. 2005; Gómez et al. 2005, 2008). Although the motions of massive stars BN and source I have been confirmed by many independent measurements of the positions of maser spots and radio continuum emission, the motion of source n has been questioned (Goddí et al. 2011). Determinations of its proper motion may be influenced by intensity variations of its bipolar radio nebula which may shift source n’s emission centroid.

Bally & Zinnecker (2005) proposed that the BN/KL explosion may have been triggered by a massive star merger or the dynamical rearrangement of a nonhierarchical system of massive stars into a hierarchical system that resulted in their ejection from the OMC1 core as high-velocity, runaway stars. In this model, the disruption and ejection of circumstellar disks and envelopes produced the BN/KL outflow. The momentum and kinetic energy of the outflow and ejected stars came from

* The final set of FITS files is only available at the CDS via anonymous ftp to cdsarc.u-strasbg.fr (130.79.128.5) or via <http://cdsarc.u-strasbg.fr/viz-bin/qcat?J/A+A/579/A130>

the release of gravitational binding energy of a compact binary formed by the dynamic interaction of three or more stars (Poveda et al. 1967; Gualandris et al. 2004; Perets & Šubr 2012; Reipurth et al. 2010; Reipurth & Mikkola 2012).

Zapata et al. (2009), Bally et al. (2011), and Goddi et al. (2011) found supporting evidence for the dynamical rearrangement model. In this scenario, the final N -body encounter would have resulted in the formation of a compact, au-scale binary, most likely source I, and the ejection of radio source I and BN, and possibly source n. However, it is still possible that additional highly-embedded IR sources will be found in dense cores such as the 1 millimeter source, SMA1 (Beuther & Nissen 2008). Some of these might contain massive stars. After all, radio source I has not yet been directly detected at any infrared wavelength.

Over 30% of massive stars are ejected from their birthplaces at high velocities (Gies & Bolton 1986). A large fraction of such runaway stars are thought to have been produced by the dynamical ejection scenario (Poveda et al. 1967). For example, a dynamical interaction is thought to have ejected the classic runaway stars μ Columbae and AE Aurigae with velocities of 108 km s^{-1} and 113 km s^{-1} , respectively, in opposite directions about $2.5 \pm 0.05 \text{ Myr}$ ago (Hoogerwerf et al. 2000, 2001; Gualandris et al. 2004). This event left behind the colliding-wind X-ray binary, ι Orionis, which is the brightest and most massive member of the $\sim 5 \text{ Myr}$ old NGC 1980 cluster located about $30'$ south of the Orion Nebula in the Orion A molecular cloud (Alves & Bouy 2012; Bouy et al. 2014).

Proper motion measurements show that the fastest components in the OMC1 fingers have a dynamic age of about 500 yr (Bally et al. 2011). However, Wu et al. (2014) used ALMA observations to argue for a somewhat older dynamic age of $<1300 \text{ yr}$ for the BN/KL outflow. Bally et al. (2011) found that the H_2 and [Fe II] finger proper motions trace-back to within a few arcseconds of J2000 = 05:35:14.5, -05:22:23 located between the current locations of radio sources I and BN. Gómez et al. (2008) found that in the Orion reference frame, the proper motions of radio sources I, BN, and n intersected within one arcsecond ($<400 \text{ au}$) of J2000 = 05:35:14.360, -05:22:28.70 about 500 yr ago, a few arcseconds from the apparent point of outflow origin determined by tracing back the near-IR proper motions of the fast ejecta.

Tan (2004) proposed an alternative scenario in which the BN object was ejected about 4000 yr ago by a dynamic interaction in the Trapezium cluster located in the center of the Orion Nebula. In this scenario, the OMC1 explosion was triggered by the serendipitous passage of the BN object through the OMC1 core. Although requiring a highly unlikely close encounter of BN with source I in the OMC1 core, Chatterjee & Tan (2012) show that the parameters of the Trapezium and BN are compatible with this scenario.

Though rare, the explosive outflow morphology of the OMC1 BN/KL outflow is not unique; other possible examples include G34.25+0.16 in the inner Galaxy (Cyganowski et al. 2008), source G in W49 (Smith et al. 2009), IRAS 05506+2414 (Sahai et al. 2008), DR21 (Zapata et al. 2013) and possibly the low-luminosity source of the molecular hydrogen outflow MHO 2714 (GGD 34) in NGC 7129 (Eisloffel 2000). However, Orion BN/KL is the nearest and least obscured, and thus most accessible for high-resolution studies. Here, we present 0.08 to 0.1 arcsec resolution images of the entire OMC1 outflow complex in the $1.64 \mu\text{m}$ [Fe II] and $2.12 \mu\text{m}$ H_2 narrow-band filters and a broad-band K_s filter obtained with adaptive optics (AO) on the Gemini South 8 m telescope. This data is combined with older AO-assisted observations obtained on Gemini North and

natural seeing-limited images acquired with a variety of other telescope to re-measure proper motions in parts of the BN/KL outflow.

2. Observations

2.1. Gemini south GeMS

The Gemini Multi-conjugate AO System (GeMS) at the Gemini South telescope on Cerro Pachon is the first and only sodium-based multi-laser guide star (LGS) AO system (Rigaut et al. 2014, 2012; Neichel et al. 2014, 2013; d'Orgeville et al. 2012). GeMS works with a LGS constellation of 5-spots: 4 of the LGS spots are at the corners of a $60''$ square, with the 5th positioned in the center. The AO bench called Canopus is mounted on one of the f/16 Cassegrain ports. Gemini South Adaptive Optics Imager (GSAOI) is a wide-field 4096 by 4096 pixel ($85''$ by $85''$ field of view) camera designed to work at the diffraction limit of the 8-m telescope in the near-IR. Three $85''$ diameter fields were observed in OMC1 between 30 December 2012 and 28 February 2013 using GSAOI. Observations of each field were obtained through 1% bandpass narrow-band filters centered on the $1.644 \mu\text{m}$ [Fe II] and $2.122 \mu\text{m}$ H_2 emission lines and the broad-band K_s filter. The corrected images have FWHM diameters of $0.08''$ to $0.1''$, providing the highest angular resolution images of the BN/KL outflow ever obtained in the near-IR.

Each field was imaged in each filter with a 5 point dither pattern to fill-in gaps between the four 2048 by 2048 pixel arrays in GSAOI. Exposure times were 43.4 s per exposure for H_2 , 43.0 for [Fe II], and 15.0 for K_s . 10 exposures were taken in each filter for a total of 430 s on-source in the narrow-band filters and 150 s in the continuum filter.

Data were processed with the Gemini GSAOI pipeline. However, additional astrometric corrections were required. Individual exposures were first registered to the Muench et al. (2002) catalog sources to acquire a world coordinate system with rms pointing error $\sim 0.1''$. A new catalog of relative star positions was generated from a preliminary aligned and co-added stack of images and used to derive a distortion map for GSAOI. The individual distortion corrected images were re-aligned and co-added to form the final mosaic in each filter.

2.2. Gemini north Altair

Between 2007 and 2009, the Gemini North 8 m telescope was used to observe the OMC1 region on three occasions using the Altair AO system with the NIRI near-IR camera through 1% narrow-band [Fe II], H_2 , and broad-band K_s filters. NIRI was used in a configuration which delivers a $40''$ field of view. In the narrow-band filters, a dithered set of five to ten 30 s exposures were obtained. A similar set of 10 second exposures were acquired in the K_s filter. In 2007, only the “ H_2 fingers” region was observed as part of the commissioning of the Altair AO system using the NIRI camera. During 2008 and 2009, we intended to image a 3×4 point grid to cover the full extent of the BN/KL outflow. However, only 5 and 8 fields were actually observed in 2008 and 2009, respectively. Only the “ H_2 fingers” field was observed during each of the three years. A summary of the observations is given in Table 1. The angular resolution of the NIRI images ranges from 0.1 to $0.2''$.

In the analysis presented here, the NIRI images were registered to the final GSAOI mosaic using IRAF tasks GEOMAP and GEOTRAN applied to unsaturated field stars. Proper

Table 1. Near-IR observations of Orion OMC1.

Year	α (J2000)	δ (J2000)	Field size	MJD	Comments
2007	05:35:12.8	-05:20:53	50'' \times 50'' at 45°	54165	H ₂ fingers; Gemini N
2008	05:35:11.9	-05:20:47	50'' \times 50'' at 45°	54753	H ₂ fingers; Gemini N
2009	05:35:11.9	-05:20:47	50'' \times 50'' at 45°	55138	H ₂ fingers; Gemini N
2013	05:35:13.2	-05:20:37	84'' \times 84'' at 0°	56290	OMC1 N; Gemini S
2013	05:35:12.5	-05:22:04	92'' \times 91'' at 0°	56323	OMC1 BN; Gemini S
2013	05:35:17.5	-05:22:48	92'' \times 91'' at 0°	56323	OMC1 SE; Gemini S

Notes. The H₂, [Fe II], and K_s images were taken on the same night.

motions were determined by marking the photocenters of features on the multi-epoch images. Images of the OMC1 outflow obtained with the Subaru 8 m telescope on MJD = 51 484 in 1999 (Kaifu et al. 2000), the Apache Point Observatory 3.5 m on MJD = 53 331 in 2004 (Bally et al. 2011) were also used. The interval between the Subaru and Gemini south observations is 4839 days.

3. Results

The 2013 epoch GSAOI images presented here reach the near-IR diffraction limit of an 8-m telescope and provide the sharpest views obtained thus far of the entire OMC1 BN/KL outflow. The combined H₂, [Fe II], and K_s color image (Fig. 1) shows H₂ fingers tipped with [Fe II] emission extending from about 30'' to 140'' from the OMC1 core. For the analysis of dynamic ages for various features, we assume that all features originated from J2000 = 05:35:14.360, -05:22:28.70 (marked with a cyan cross in Fig. 2), the suspected location from which the BN object and radio source I were ejected about 500 yr ago (Gómez et al. 2008) and within a few arc seconds of the suspected point of origin of the fingers determined from the intersection point of the proper motion vectors (Bally et al. 2011). Figure 2 shows the H₂ image with the location of BN, I, an n shown along with their proper motions.

The two brightest [Fe II] bow shocks correspond to the Herbig-Haro objects HH 201 and HH 210 located 60'' northwest and 113'' north of OMC1 (Gull et al. 1973; Münch & Taylor 1974; Canto et al. 1980; Axon & Taylor 1984). These shocks are visible on ground-based and *Hubble* Space Telescope images in [O I], H α , [N II] and [S II]. However, they only exhibit faint H₂ emission (Graham et al. 2003), indicating that they lie in the mostly atomic, photon-dominated region (PDR) located between the Orion Nebula's ionization front and the background Orion A molecular cloud and OMC1 cloud core. The most prominent H₂ fingers consist of multiple [Fe II] finger-tips trailed by H₂ wakes with an orientation of PA \sim 340° to 350°. This chain of shocks and wakes extends from about 50'' to 135'' from the ejection center. It consists of at least a dozen nested H₂ bow shocks tipped with [Fe II] emission regions. The brightest [Fe II] features are visible in the visual-wavelength emission lines commonly seen in Herbig-Haro objects such as [O I], [S II], [N II], and H α and have been designated as HH 205 through 209. These HH objects are associated with the tips of the chain of H₂ wakes propagating toward position angle (PA) \sim 340° to 350°.

More than 120 distinct wakes are visible in the 2.12 μ m H₂ images that exhibit nearly parallel walls and large proper motions along their axes (Bally et al. 2011). Figure 3 shows a median filtered version of the 2013 GSAOI H₂ mosaic created by convolving the image with a 51 pixel kernel (1''; each pixel is 0.02'' on a side) using the IRAF function MEDIAN, and subtracting the result from the original image. Vectors were

drawn from the suspected ejection site of radio sources BN and I (the coordinates are given above) to each H₂ or [Fe II] fingertip. The dashed vector near the top marks a chain of H₂ knots and bow shocks with proper motions nearly orthogonal to the northern fingers; this feature traces another flow originating east of the imaged field. This flow is also seen faintly at visual wavelengths. The H₂ emission becomes too confused within \sim 30'' of the suspected ejection location due to multiple overlapping features. The natural seeing-limited 1999 epoch Subaru telescope image from Kaifu et al. (2000) and the 2005 epoch image from Bally et al. (2011) were used to trace a few additional H₂ fingers beyond the boundaries of the GSAOI image in the southwest portion of Fig. 3.

In the northwestern part of the flow, the H₂ wakes range in diameter from 2'' to 8'' (7×10^{14} to 3×10^{15} cm) with limb-brightened rims less than 1'' ($<3 \times 10^{14}$ cm) wide (Fig. 4). The half dozen major finger clusters in the northwest are up to 60'' (\sim 0.1 pc) long. The wakes in the inner part of the flow are narrower, tend to be shorter, and are more numerous resulting in a high degree of overlap along the line-of-sight. The H₂ emission tends to be fainter or disappears near the wake-tips where it is replaced by [Fe II] emission.

Most of the [Fe II] emission in the BN/KL outflow originates from the fingertips which are faint or invisible in H₂. Dozens of fingertips are visible in the 1.64 μ m [Fe II] line. The two blue vectors in Fig. 3 point to the two brightest [Fe II] features which are also bright in visual wavelength shock-excited emission lines such as [O I] and [S II] and are designated as HH 201 and 210. These fingertips are very faint in H₂. Figure 4 shows a color version of the “H₂ fingers” region in 2013 from GSAOI showing H₂ (red), [Fe II] (green), and the broadband light in K_s (blue).

3.1. Proper motions of selected knots

Previous analyses of multi-epoch ground-based images have shown that the highest proper motion knots in the BN/KL outflow are most distant from OMC1 (Jones & Walker 1985; Lee & Burton 2000; Bally et al. 2011). Figure 5 shows a difference image obtained by subtracting the 1999 epoch Subaru H₂ image of Kaifu et al. (2000) from our 2013 GSAOI H₂ image. Although the registration of the two images is not perfect due to small-scale distortions in the Subaru image (this image was assembled from a mosaic of smaller images), the overall pattern of expansion away from the OMC1 core is obvious.

Comparison of the 2013 epoch images in the sub-field containing the brightest part of the PA \sim 340° to 350° finger with 2007, 2008, 2009 Gemini North NIRI images show large proper motions of the [Fe II]-dominated fingertips pointing away from the OMC1 core. This field contains several compact, high velocity H₂ knots with sub-arcsecond to arcsecond diameters and proper motions similar to the [Fe II] fingertips. Additionally, the H₂ wakes are expanding at right angles to a line connecting the

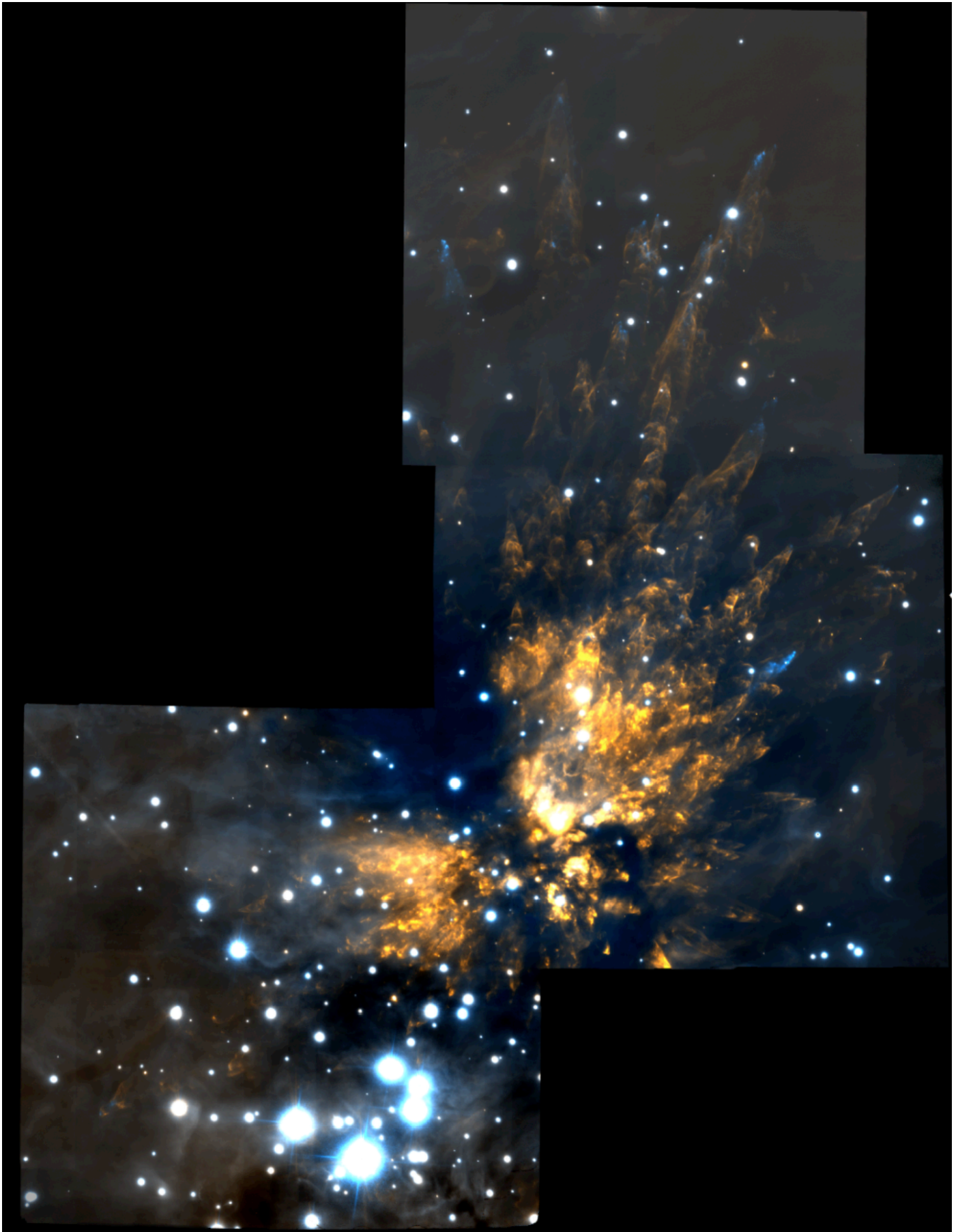


Fig. 1. Wide-field image showing the OMC1 outflow in H₂ (orange) and [Fe II] (cyan).

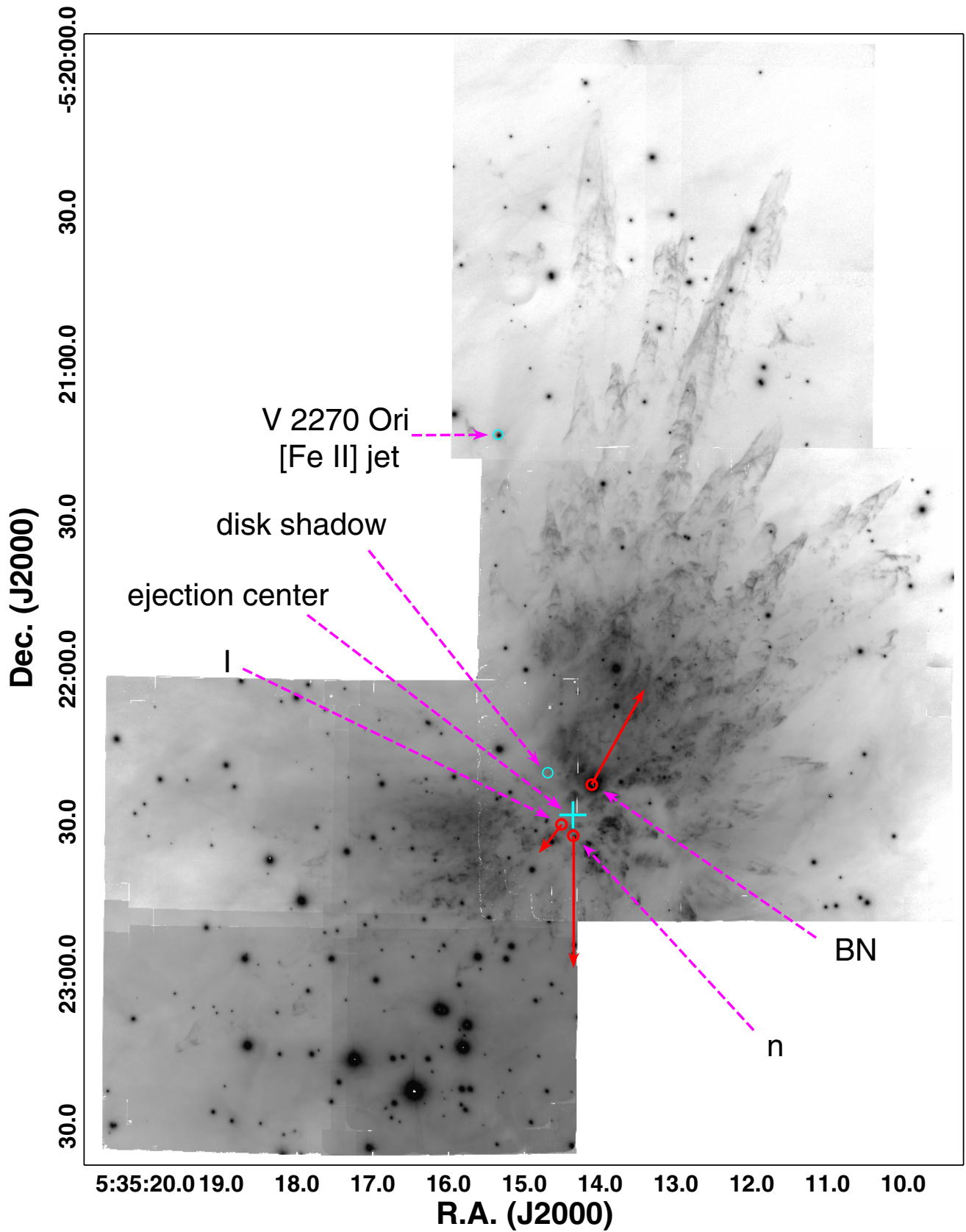


Fig. 2. Wide-field image showing the OMC1 outflow in H₂ with proper motions of the BN object, radio source I, and radio source n superimposed. The lengths of the red-solid vectors are proportional to the motions measured by Gomez et al. (2008) with the lengths of the vectors in arcseconds equal to the motion in km s⁻¹ (e.g. 10'' corresponds to a motion of 10 km s⁻¹). The ejection center as determined by radio proper motions is shown by a cross. The locations of the disk shadow shown in Fig. 18 and the source of the [Fe II] jet shown in Fig. 17, V2270 Ori, are indicated.

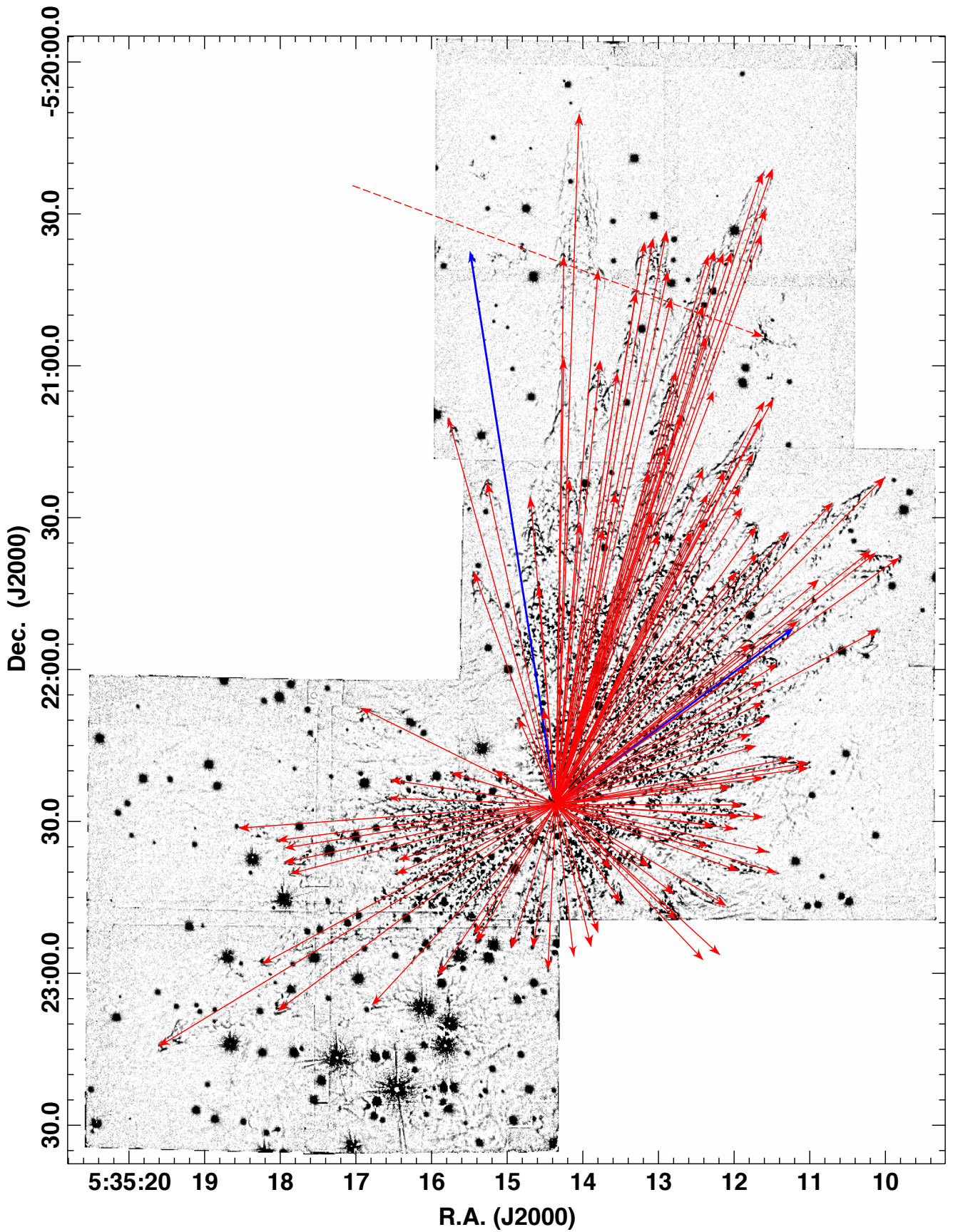


Fig. 3. Outer system of fingers (vectors) in the $2.122 \mu\text{m}$ H_2 GSAOI image. The dashed vector shows the background flow whose motions are towards the west. The blue vectors mark the direction from the explosion center to the two $[\text{Fe II}]$ – dominated shocks, HH 201 and HH 210. The background image has been median filtered as described in the text.

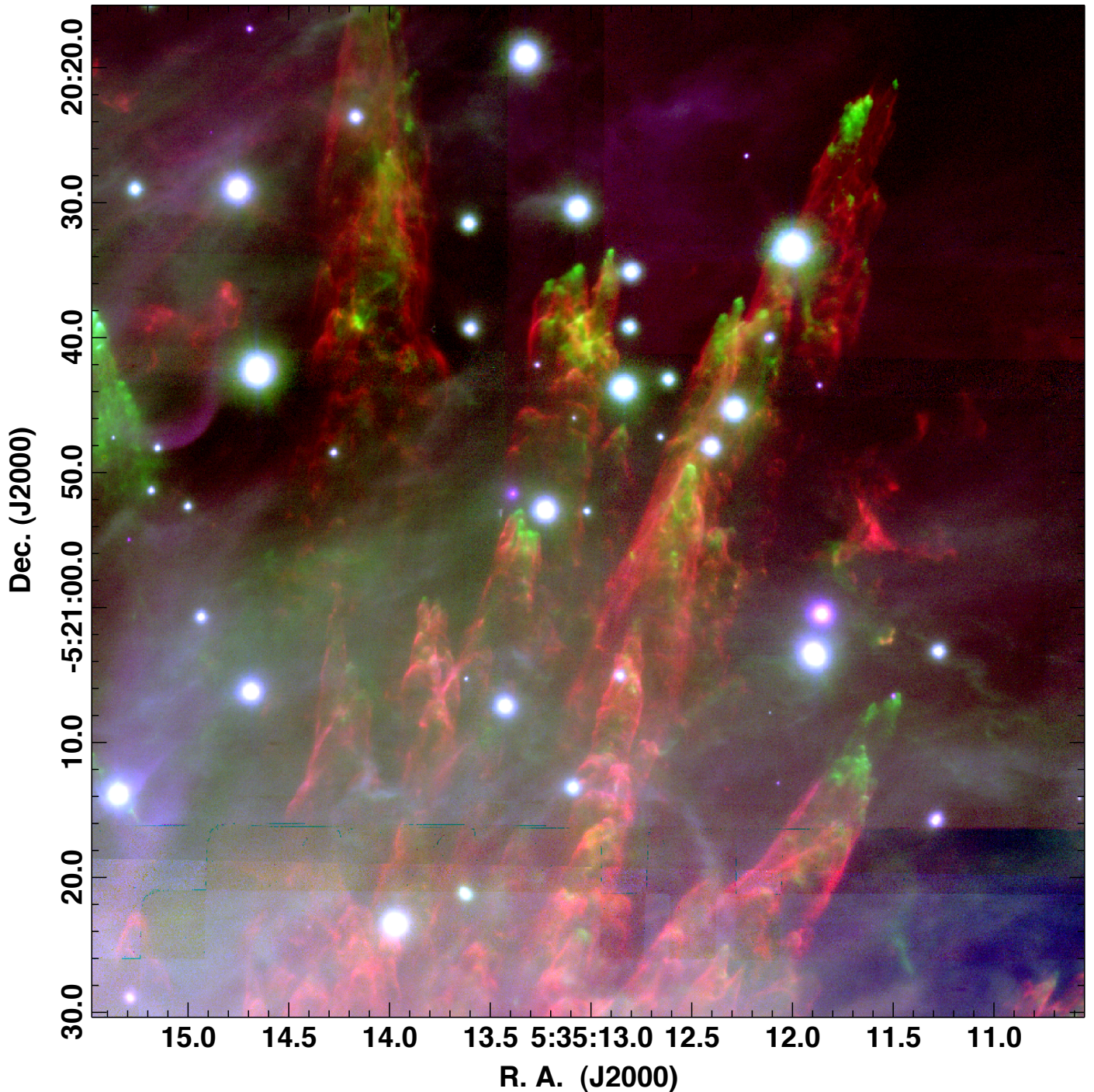


Fig. 4. K_s image (blue), the $1.644 \mu\text{m}$ [Fe II] image (green), and $2.122 \mu\text{m}$ H_2 (red) in the “ H_2 fingers” field using the GSAOI 2013 data.

fingertips to OMC1. The fastest transverse proper motions are found close to the fingertips and decline along the parts of the wake closer to OMC1.

The most reliable proper motions were measured in this field using the AO-assisted images from 2013 and 2007 that are separated by 2125 days. Figure 4 shows a color composite image of this field. Figures 6 and 7 show difference images in H_2 and [Fe II] formed by subtracting a de-distorted, intensity matched and registered 2013 GSAOI images from the corresponding 2007 NIRI images. Figures 8 and 9 show closeup views of the central part of the field shown in Figs. 6 and 7 that contains a bright bow shock. These images show 200 to 300 km s^{-1} proper motions of the fingertips in both H_2 and [Fe II].

Figure 8 shows that in addition to the large proper motions of the fingertips, the H_2 wakes are spreading with velocities ranging from less than 20 to about 80 km s^{-1} in a direction orthogonal to the motions of the fingertips. The two regions marked W1 and W2 show the locations of slow and fast transverse spreading, respectively. The amount of transverse motion between the two epochs at these two locations are indicated by the closely spaced dashed lines. The spreading velocity decreases with increasing distance from the fingertips. Figure 9 demonstrates that these spreading H_2 regions are located behind a fast-moving [Fe II] bullet whose locations in 2007 and 2013 are indicated.

The closeup H_2 images of this region (Figs. 6 and 8) show a high-velocity compact clump (HVCC) which exhibits a proper

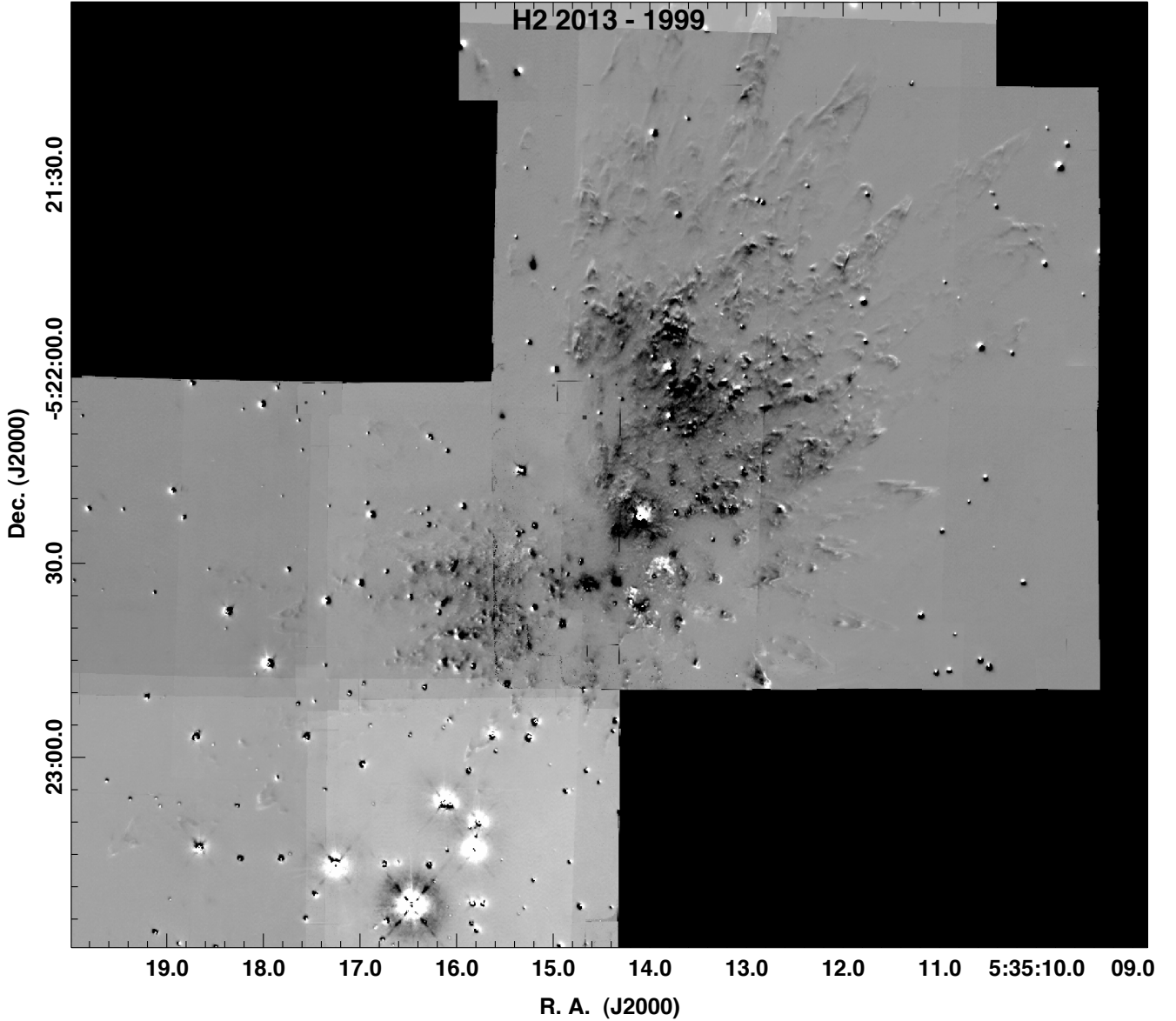


Fig. 5. A $2.122\ \mu\text{m}$ H_2 difference image showing proper motions in the field imaged by Kaifu et al. (1999) with the Subaru telescope in 1999. The images shows the difference between 2013 and 1999 epoch data. Residual distortion corrections result in imperfect registration.

motion of $V_{\text{HVCC}} = 300 \pm 20\ \text{km s}^{-1}$ over the 6 yr ($1.85 \times 10^8\ \text{s}$) interval between the acquisition of the Gemini North and South images in 2007 and 2013. This HVCC is located at projected distance of $100''$ from the current location of source I and $d_{\text{ejection}} = 97''$ ($0.195\ \text{pc}$) from the suspected location of sources I and BN more than 500 yr ago prior to their dynamic ejection. Assuming no deceleration, the dynamic age of this knot is $t_{\text{dyn}} = d_{\text{ejection}}/V_{\text{HVCC}} \approx 640 \pm 30\ \text{yr}$ (see Table 2). Comparison of HST images in [O I] and [S II] taken on MJD 50 170 show that the HVCC is located about $5''$ south of HH 207 which is also bright in our [Fe II] images. In [Fe II], HH 207 has a proper motion of $229\ \text{km s}^{-1}$ (Table 2). Measured on *Hubble Space Telescope* images in the visual wavelength range, HH 207 had proper motions of $167\ \text{km s}^{-1}$ in [S II], $203\ \text{km s}^{-1}$ in $\text{H}\alpha$, and $291\ \text{km s}^{-1}$ in [N II] (Doi et al. 2002). Using the velocity difference between the H_2 and [Fe II] proper motions of the HVCC and the [Fe II] emission associated with HH 207 ($\sim 68\ \text{km s}^{-1}$) and the current projected separation of $5''$ indicates that the HVCC may catch up to the moving [Fe II] emission region in

about 140 yr (assuming that they are not displaced along the line of sight).

Figure 8 shows that this HVCC has undergone considerable transverse spreading over the past 6 yr. The HVCC is either subject to photometric variations or experiencing significant “side-ways splashing” of post-shock material. The morphological evolution of the HVCC suggests that it may have been decelerated significantly from its ejection velocity. Several less-prominent HVCCs exhibit motions of $200\text{--}300\ \text{km s}^{-1}$. Measured motions of a sample (subset) of fingertips, H_2 wakes, and compact, fast knots are given in Table 2.

While the fingertips with 100 to $300\ \text{km s}^{-1}$ motion (best seen in [Fe II]) are moving along a direction which points directly away from the OMC1 core, the H_2 wakes behind each [Fe II] feature are spreading at right angles to the fingertip proper motions. The wake spreading-velocities tend to decrease with increasing distance behind each fingertip. Within a few arcseconds of the fingertips, some H_2 wakes show transverse expansion as fast as $80\ \text{km s}^{-1}$ orthogonal to the wake orientation and

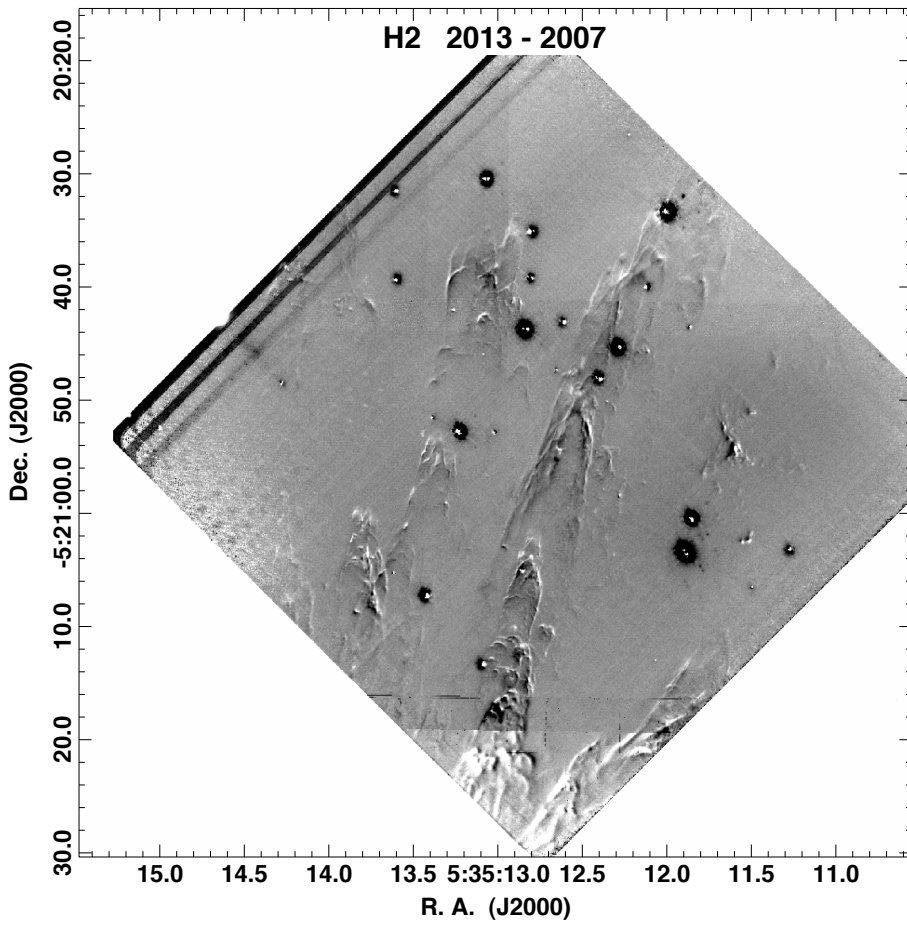


Fig. 6. A $2.122 \mu\text{m}$ H_2 image showing proper motions in the “ H_2 fingers” field. The image shows the difference between images obtained in 2013 with Gemini S using GSAOI and in 2007 with Gemini N using NIRI.

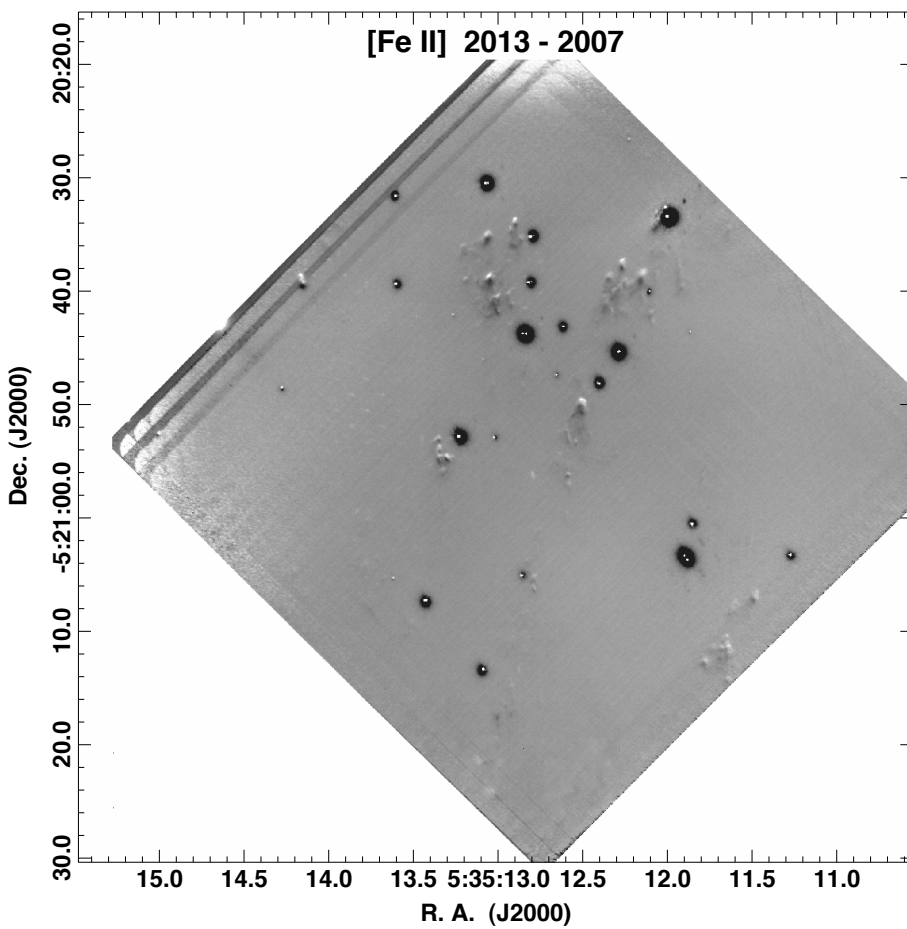


Fig. 7. A $1.644 \mu\text{m}$ $[\text{Fe II}]$ image showing proper motions in the “ H_2 fingers” field. The image shows the difference between images obtained in 2013 with Gemini S using GSAOI and in 2007 with Gemini N using NIRI.

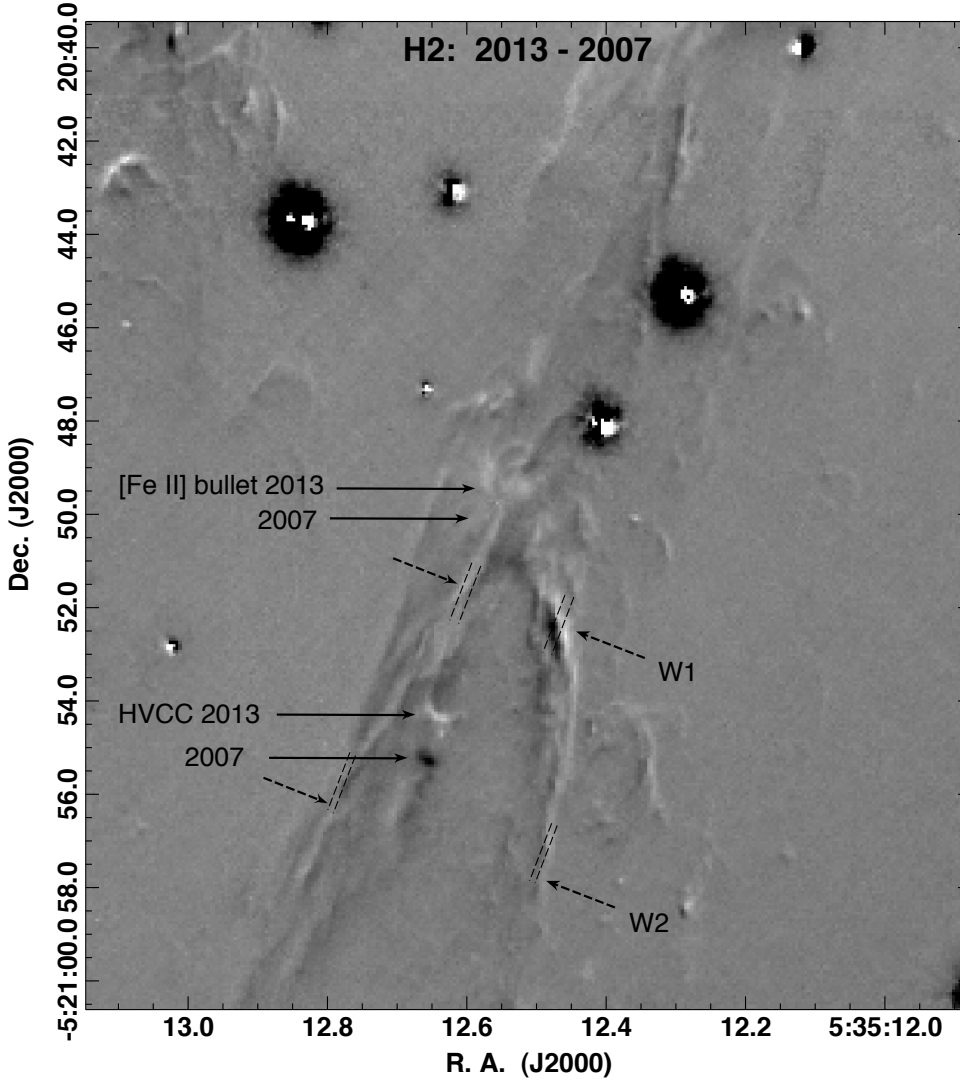


Fig. 8. Closeup view of the main H₂ finger and the HVCC in the “H₂ fingers” field showing the difference between images obtained in 2013 with Gemini S using GSAOI and in 2007 with Gemini N using NIRI.

proper motion of the fingertip. Spreading speeds decline to under 20 km s^{-1} (the measurement limit) at distances of more than $10''$ to $15''$ behind the fingertip.

The transverse spread is consistent with a simple model of a disturbance created by the passage of a high density compact object through the medium as shown below by numerical simulations. Let y be the distance from the tip of a finger to the location where the wake half-width (width of the wake divided by 2) and transverse expansion speed are measured. The ratio of the transverse spreading-velocity, $V_{\text{perp}}(y)$ (one-half of the velocity with which the two sides of a wake are moving apart) to the fingertip proper motion, V_{PM} , is comparable to the half-width of the wake at a given location, $X_{\text{perp}}(y)$, divided by the distance of that location from the fingertip, $Y_{\text{PM}}(y)$. Thus, $V_{\text{perp}}(y)/V_{\text{PM}} \approx X_{\text{perp}}(y)/Y_{\text{PM}}(y)$. Both the fingertip and spreading velocities are highly supersonic.

As shown by previous ground-based measurements, the largest proper motions are seen at the largest projected distance from the OMC1 core and the suspected locations of the BN object and radio source I about 500 yr ago. The northwestern fingertips located at the greatest distance from the OMC1 core exhibit the largest proper motions (200 to over 300 km s^{-1}) and tend to show a pattern of increasing maximum velocity with increasing distance from the core. However the region also contains a number of slower-moving features with proper motions ranging from under 100 to about 200 km s^{-1} . It is likely that

these features have experienced significant deceleration as they interact with the surrounding medium. The fastest knots and fingertips have dynamic ages consistent with ejection between 450 and 600 yr ago.

Doi et al. (2002) measured visual wavelength proper motions for Herbig-Haro (HH) objects protruding into the PDR behind the Orion Nebula. Two of the brightest [Fe II] features correspond to HH 201 northwest of OMC1 and 210 north of OMC1. Doi et al. (2002) measured proper motions of 312 to 315 km s^{-1} for various components of HH 201 and 309 to 425 km s^{-1} for knots in HH 210. Grosso et al. (2006) detected X-rays from the wake of HH 210, which is the highest proper motion finger in the OMC1 outflow and one of the relatively few visible at visual wavelengths, thereby demonstrating that at least some of the fingers contain hot, X-ray emitting plasma. Additional HH objects are associated with the Orion fingers including HH 205 to 209, and HH 601 to 607 with proper motion velocities ranging from 100 to 300 km s^{-1} (Doi et al. 2002). All of these features have large negative radial velocities. For example, HH 201 has $V_{\text{LSR}} \sim -260$ to -284 km s^{-1} (Doi et al. 2004).

3.2. Constraints on the ejection mechanism

A number of models have been proposed to explain the [Fe II] fingers and H₂ wakes in the BN/KL outflow. The fingertips

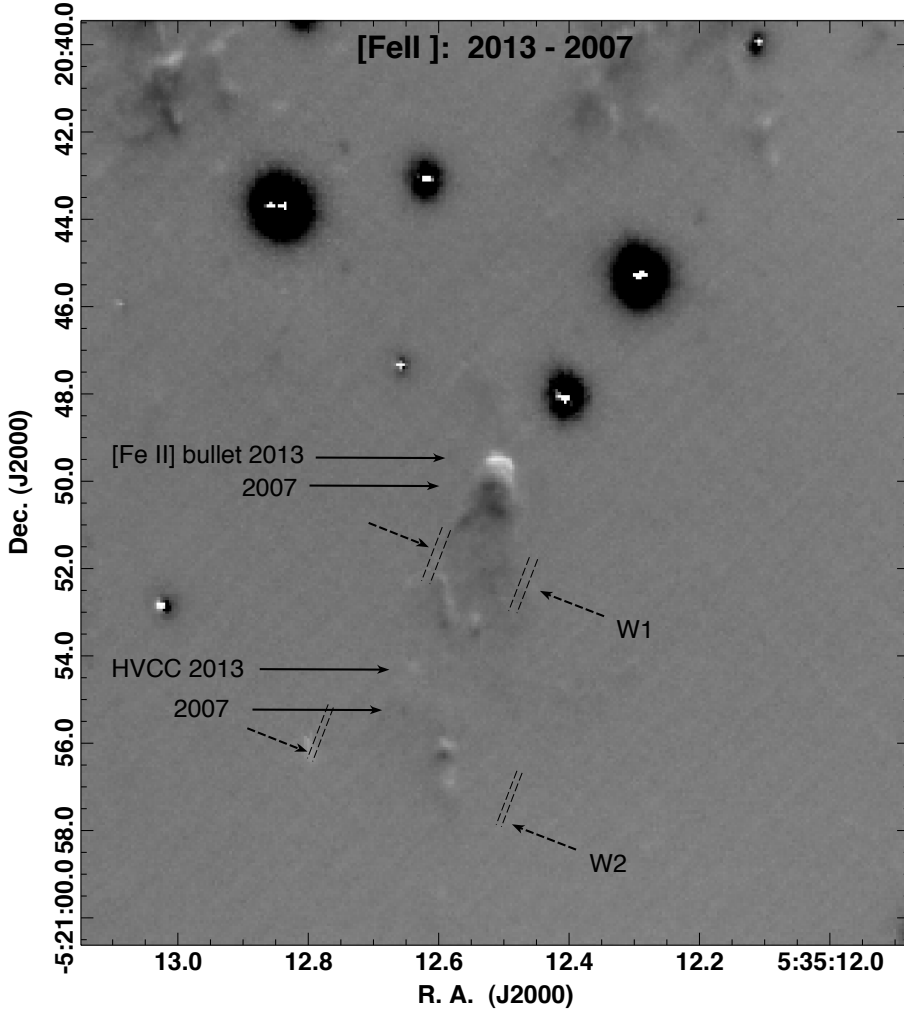


Fig. 9. Same as Fig. 7 but for [Fe II].

contain [Fe II] knots and bow shocks with diameters of $1''$ (~ 400 au) or less, estimated by measuring the separation between points where tangent lines on the leading edges of the shock on either side of the tip are at an angle of 90° with respect to each other. This dimension is used as an estimator for the size-scale of the material powering each shock which may be the working surface of a jet (Smith & Rosen 2007), a wind which has experienced instabilities (Stone et al. 1995), or a dense bullet (Allen & Burton 1993). The tangent lines become increasingly parallel (greater than 90°) in the wake. Most of these [Fe II] bullets and the H_2 HVCCs are located more than $100''$ from their ejection site.

The individual fingers resemble the shocks produced by accretion-powered jets or collimated flows powered by young stellar objects (YSOs) as they sweep up the ambient medium (Reipurth & Bally 2001). However the presence of many dozens of individual fingers and over 100 shocks with similar dynamic ages moving away from the OMC1 core in all directions suggests that a single, brief event is more likely.

The multitude of fingers and wakes could be powered by a fast wide-angle wind which experienced instabilities and broke into a multitude of protrusions (Stone et al. 1995; McCaughrean & Mac Low 1997). Rayleigh-Taylor (RT) instabilities can produce fingers of fast ejecta surrounded by slower clumps of dense gas if the wind velocity increases with time on a time-scale shorter than the crossing time of the wind in the wind-dominated region. Alternatively, a steady wind running into a stationary medium with a density profile decreasing faster than r^{-2} can

be subject to RT instabilities. Neither an accelerating wind, nor a wind running into a rapidly decreasing density gradient is expected to produce the approximately Hubble-flow type behavior with the maximum velocity of the ejecta increasing linearly with increasing projected distance from the source.

The fingers and wakes may be driven by high-density, compact ejecta (“bullets” or HVCCs) as originally suggested by Allen & Burton (1993). Similar bullets have been detected in other astrophysical contexts such as supernova remnants where hydrodynamic and cooling instabilities fragment an expanding stellar envelope (Fesen et al. 2011; Milisavljevic & Fesen 2013).

Assuming the ejection occurred ~ 500 yr ago at approximately the location of the BN/KL infrared nebula (Bally & Zinnecker 2005; Zapata et al. 2009; Bally et al. 2011; Goddi et al. 2011), the most distant knots to the northwest provide the most stringent constraints on the ejecta properties. These knots have traveled ~ 0.28 pc in projection in ~ 500 yr. Thus, the time-averaged velocities must be greater than ~ 550 km s^{-1} . For an explosive origin, the fingertip proper motions should increase linearly with increasing distance from the launch region. While a few H_2 features have proper motions between 300 and 350 km s^{-1} , most show lower velocities, especially closer to the OMC1 core. Because the faster motions are at least 20% slower than expected for a 500 yr-old explosion, the ejecta have either decelerated or were ejected earlier. The absence of faster ejecta in [Fe II] and H_2 could be a consequence of deceleration, an older time of ejection, or a selection effect resulting from excitation conditions in the shocks. [Fe II] can be excited into higher

Table 2. Selected OMC1 bullets and bow shocks.

Feature	α (J2000) (05 ^h 35 ^m +)	δ (J2000) (-5° +)	ΔX (")	V (km s ⁻¹)	PA (°)	D (")	τ_{dyn} (yr)	Comments
H ₂ 1	12.625	20:55.22	0.88	297	346	97	643	HVCC H ₂ knot
2	12.058	20:37.68	0.43	145	324	116	1577	Ahead of H ₂ ^a
3	12.270	20:37.82	0.84	283	344	114	794	"
4	12.351	20:38.84	0.54	182	350	112	1213	"
5	12.965	21:16.37	0.33	111	338	74	1314	Cluster NE of H ₂ ^a
6	12.989	21:17.73	0.53	179	347	73	801	"
S1	11.532	21:02.24	0.30	101	233	–	–	Background flow
S2	11.616	20:53.94	0.29	98	227	–	–	"
S3	11.614	20:54.45	0.54	182	218	–	–	"
W1	12.543	20:52.03	0.240	80	–	–	29	Spreading H ₂ wake
W3	12.642	20:56.45	0.138	46	–	–	100	"
[Fe II] 1	12.521	20:50.12	0.68	229	345	102	863	HH 207; Fe II] bow
2	12.165	20:39.09	0.81	273	345	116	835	
3	12.274	20:37.96	0.79	267	354	114	839	
4	12.353	20:38.94	0.55	186	349	112	1184	
5	12.898	20:34.12	0.59	199	1	116	1146	
6	12.932	20:34.87	0.61	206	3	115	1097	
7	13.066	20:35.39	0.61	206	355	114	1088	
8	13.052	20:39.01	0.61	206	354	112	1069	
9	13.010	20:40.81	0.56	189	350	97	1009	
10	13.308	20:54.78	0.41	138	354	96	1367	
11	13.386	20:56.16	0.53	179	353	95	1043	
12	13.354	20:53.14	0.33	111	357	98	1736	
13	12.592	20:56.23	0.27	91	354	97	2096	
14	12.795	21:05.50	0.49	165	354	87	1036	
15	11.502	21:07.20	0.92	310	338	94	596	
16	11.680	21:10.86	0.71	240	326	89	729	
17	11.792	21:12.81	0.41	138	329	86	1225	

Notes. ^(a) The projected distance from the suspected point of ejection of the stars BN and source I about 500 yr ago, D , is measured from J2000 = 05:35:14.35, -5:22:28.5 (Gomez et al. 2008).

ionization stages and H₂ may be dissociated above a critical shock speed. Such ultra-fast material should still be revealed by their H₂ wakes.

If the bullets originated between radio sources I and BN, they moved between 10² to 10³ times their current diameters to their present location. The HVCC shown in Fig. 8 had a diameter about about 0.2" (100 au) in 2007 and traversed a distance of about 100", about 500 times its own diameter, from the suspected ejection site between sources I and BN. Assuming that they are moving ballistically and not actively powered by jets or winds, momentum conservation requires that such bullets must be ~500 times denser than the environment. Such bullets are unlikely to contain sufficient mass to be bound by their self-gravity. They may be confined by ram pressure, otherwise they are likely to be expanding with a speed comparable to their internal sound speeds.

If the bullets were formed from the disruption of circumstellar disks or envelopes within tens of au of the massive stars ejected from the OMC1 cloud core, their initial densities are expected to be $n(\text{H}_2) \sim 10^{10}$ to 10^{15} cm⁻³, comparable to the densities of disks and inner envelopes. Following dynamic ejection, bullets are likely to expand with a velocity comparable to their an internal sound speed c_s . In the absence of ram-pressure confinement by the medium the bullet is likely to sweep out a conical region given by the Mach angle, $M \sim 2c_s/V_B$ where V_B is the bullet velocity. Using the observed sizes of the compact [Fe II] and H₂ knots (40 to 400 au) and a distance greater than 0.2 pc from the ejection site implies $c_s < 0.6$ km s⁻¹ consistent with an H₂ temperature of ~10² K. Although expansion will tend to cool the bullets below the surrounding medium, the intense IR radiation from OMC1 and heating by shock radiation

will tend to keep them warm. It is likely that many bullets are moving into regions already shocked, heated, and partially evacuated by faster, previously ejected material. Such clumps will interact with a post-shock medium having a lower-density than the ambient medium, making it more likely for the bullets to be in free-expansion rather than being confined by ram pressure.

The properties of the H₂ wakes constrain the density of the medium into which the suspected HVCCs are moving. The wakes have widths that are an order-of-magnitude wider than the H₂ HVCCs and [Fe II] fingertips (2" to 10" with most being near the lower-end of this range). Their formation requires that the heated layer behind the forward shock moving into the ambient medium has a cooling length larger than the clump (or the width of the jet beam; Blondin et al. 1990). Figure 10 shows a cartoon of a dense bullet moving through a medium. A forward shock-heated ambient medium streams around the moving clump and drives lower-velocity shocks sideways into the ambient medium. A much slower, reverse shock propagates into the clump and compresses its leading edge.

The post-shock temperature immediately behind a shock is given by $T_{\text{ps}} = 3\mu V_s^2/16k$ where V_s is the shock speed. Blondin et al. (1990) give the cooling distance as $d_{\text{cool}} = V_s t_{\text{cool}}/4 = 9\mu V_s^3/64n_0\Lambda(T_{\text{ps}}) \approx 4.5 \times 10^{16} V_{100}^{4.0}/n_0$ where μ is the mean molecular weight of the pre-shocked gas particles, $\Lambda(T_{\text{ps}})$ is the cooling function, V_{100} is the shock velocity in units of 100 km s⁻¹, and n_0 is the pre-shock particle density. More recent numerical studies of the cooling function give $d_{\text{cool}} \approx 5.5 \times 10^{17} V_{100}^{4.4}/n_0$ for $80 \text{ km s}^{-1} < V_s < 1200 \text{ km s}^{-1}$ (Draine 2011). Thus, a $V_s = 300 \text{ km s}^{-1}$ shock moving into a density $n_0 = 10^4 \text{ cm}^{-3}$ has a cooling length $L_{\text{cool}} \sim 7 \times 10^{15} \text{ cm}$ (470 au). Thus, for ambient medium densities between 10^3 cm^{-3}

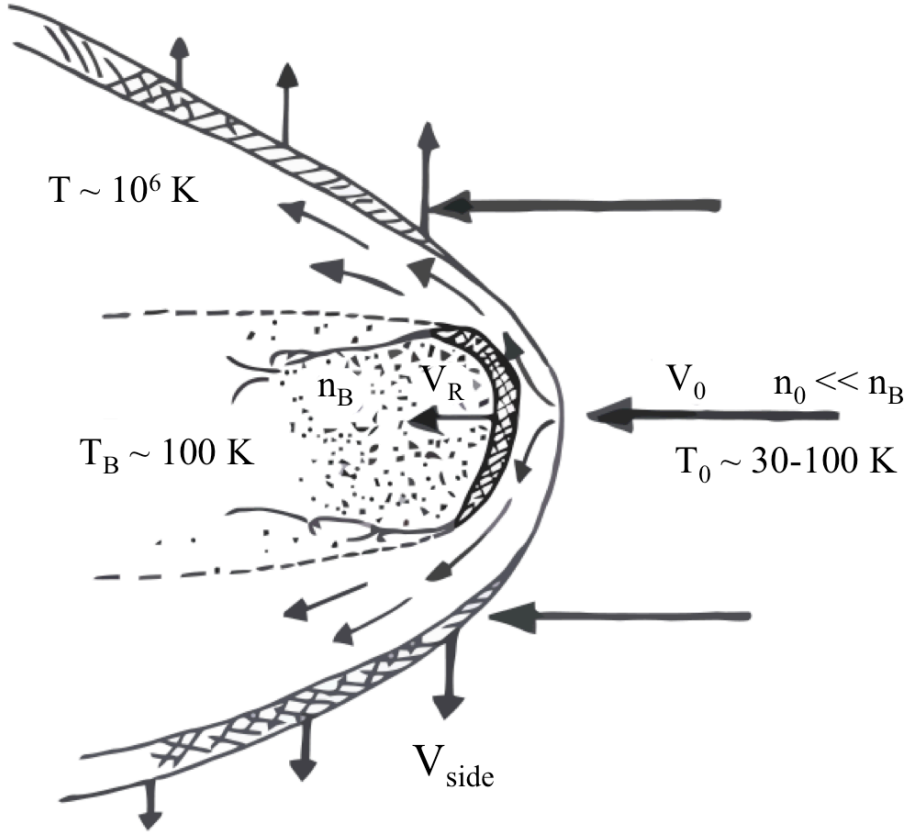


Fig. 10. Cartoon showing the shock structure formed by a hypersonic, dense bullet moving through a cold medium. The flow vectors are shown in the rest-frame of the bullet. The forward shock velocity V_0 is nearly identical to the bullet velocity and heats the post-shock ambient medium to at temperature $\sim 10^6$ K. The reverse shock propagated back into the bullet with a speed $V_R \sim V_0(n_0/n_B)^{1/2}$, where n_0 is the density of the ambient medium and n_B is the bullet density. The transverse expansion of the hot, high-pressure, post-shock medium sweeps-up the colder, lower-pressure ambient medium to form the H_2 wake. Only the transverse component of the vector V_{side} is shown. The fluid velocity of the material swept-up by the expansion of the hot, shocked ambient medium is the vector sum of the pre-shock ambient medium (as seen in the reference frame of the bullet), and the velocity of the sideways splash produced by the expanding hot plasma.

and 10^4 cm^{-3} typical for the “Integral Shaped Filament” in the Orion A molecular cloud located behind the Orion Nebula, these cooling lengths correspond to $1.1''$ to $11''$ at the distance of Orion, and are larger than the HVCCs and [Fe II] knots.

For a dense HVCC driving a forward shock into the medium with speeds of 150 to 500 km s^{-1} , the hot (~ 1 to 10 MK) plasma will splash sideways to produce a wide bow-shaped wake. In the OMC1 rest frame the 30 to 300 yr cooling time corresponds to a wake-length $L_{\text{wake}} \sim 3 \times 10^{16}$ to $3 \times 10^{17} \text{ cm}$, the latter being comparable to the lengths of fingers in the north and west parts of the OMC1 outflow. The sideways expansion of the hot plasma into the surrounding medium can then drive a slower ($V_{\text{side}} < 100 \text{ km s}^{-1}$) side shock. The H_2 emission is likely to be produced in the swept-up, compressed, and shock heated layer behind the shock. However, intense UV radiation produced by the shock hot plasma may also excite H_2 molecules outside the wake, resulting in fluorescent excitation.

The reverse shock propagating back into a dense bullet will be much weaker than the forward shock owing to the bullet’s higher density. For a forward shock moving into a medium with density n_0 with velocity V_S , the speed of the reverse shock moving into the bullet having a density n_B (in the frame of the bullet) is $V_B \sim V_S(n_0/n_B)^{1/2}$. For a density contrast ratio $n_B/n_0 \approx 10^3$, the reverse shock propagating back into the bullet will have speed $V_B \sim 0.03V_S = 10 \text{ km s}^{-1}$ for a forward shock speed of 300 km s^{-1} .

3.3. Numerical modeling

We use the Eulerian adaptive mesh refinement (AMR) hydrodynamics + N -body code, Enzo (Bryan et al. 2014) to model the propagation and evolution of bullets and the shocks they produce as they migrate through the ambient. The simulation set up is analogous to that of Silvia et al. (2010, 2012) in which an

over-dense, spherical cloud is embedded in a uniform ambient medium. For the simulation presented here, we have assumed an adiabatic equation of state that ignores any effects radiative cooling may have in this scenario. More detailed calculations using a realistic cooling curve for the post-shock gas will be presented in a future paper.

In order to track the largest possible head-tail structure as the cloud is disrupted, without losing information due to flows that might exit the computational domain, we give the ambient medium a uniform velocity such that it washes over the cloud, rather than moving the cloud itself. As the medium flows past the cloud, it drives shocks into the cloud interior and ablates material from the cloud-medium interface – producing a tail of material that is carried downstream. In order to capture the evolution of the cloud over a large physical volume while minimizing the computational cost of the simulation, we use a coarse-resolution root grid with a physical cell size of $\sim 78 \text{ au}$ per cell and eight levels of adaptive mesh refinement such that the cloud structure is resolved at a peak resolution of $\sim 0.3 \text{ au}$ per cell. The full computational volume is $7500 \times 2500 \times 2500 \text{ au}$.

Figure 11 shows a comparison between one of the H_2 fingertips and the numerical model showing the density structure of a dense, supersonic cloud that has moved approximately 500 times its initial diameter through a uniform medium. At the start of the simulation, the medium is initialized with a number density of $n = 10^3 \text{ cm}^{-3}$, a temperature of $T = 20 \text{ K}$, and uniform velocity of $v = 250 \text{ km s}^{-1}$ directed along the x -axis of the simulation domain. The cloud is initialized with a density 10^4 times higher than that of the ambient medium, a temperature of 100 K , and a radius of $r = 10 \text{ au}$.

Figures 12 through 16, made using the yt toolkit (Turk et al. 2011), show the density, x, y, z -velocity structure, and temperature of the bullet after 100 yr of evolution. For this simulation, the initial velocity of the cloud with the respect to the medium is

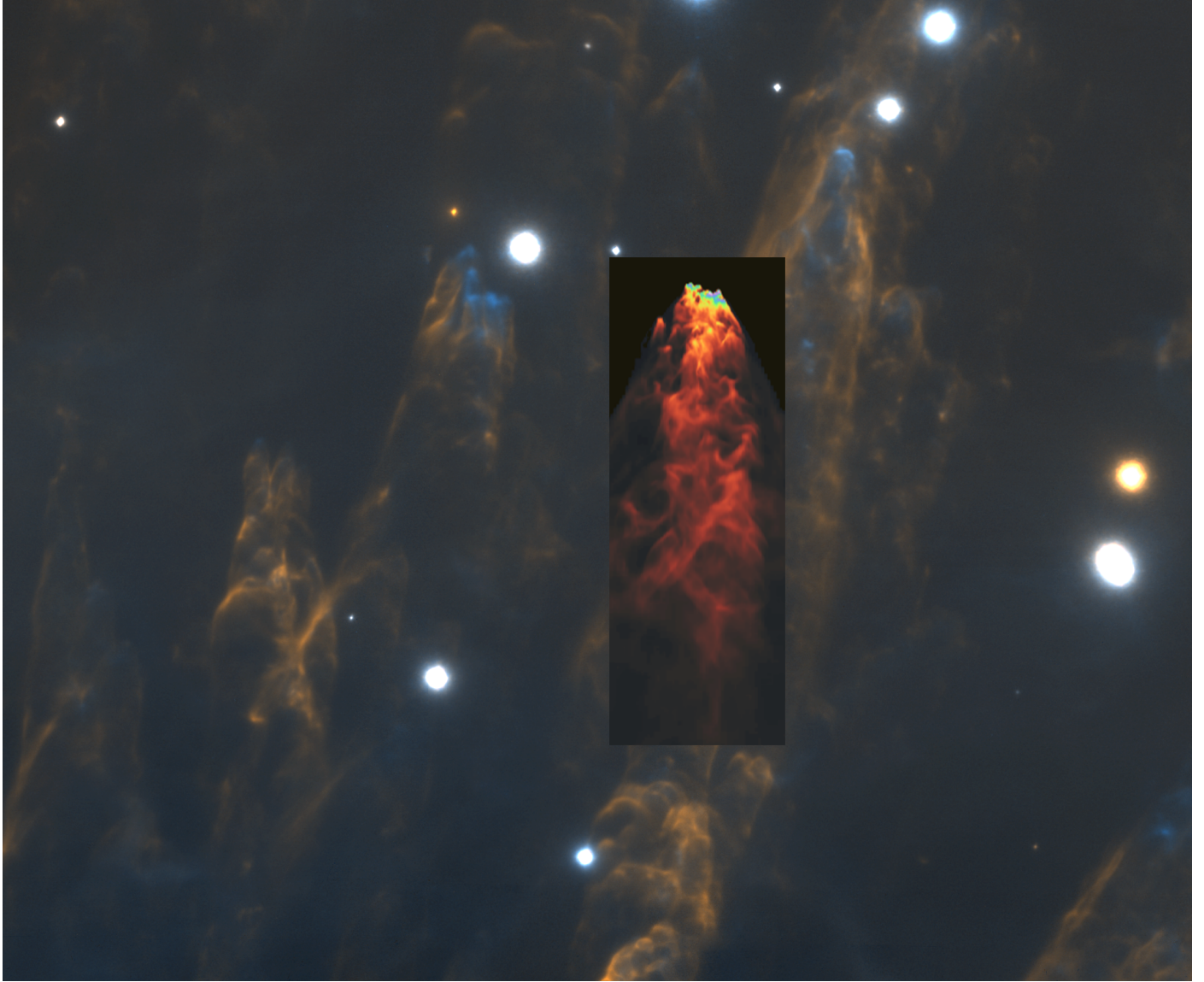


Fig. 11. Numerical simulation of a spherical object with a density 10^3 times higher than the background density, moving with a velocity 10^3 times faster than the sound speed in the medium. The frame shows the projected density distribution after the objects has moved about 10^3 times its initial diameter. The simulation projection is superimposed next to one of the fingers shown in Fig. 1.

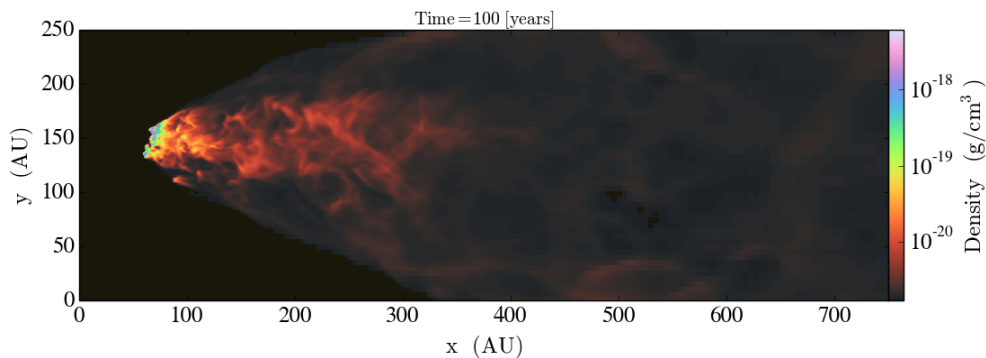


Fig. 12. Density-weighted projection of gas density from the Enzo simulation described in Sect. 3.3 at $t = 100$ yr. Projected values are computed such that $\rho_{\text{proj}} = \frac{\sum_i \rho_i^2}{\sum_i \rho_i}$ where ρ_i is the density, i denotes the cell number, and ρ is the density in cell i .

too slow to reach the observed positions given an ejection 500 yr ago, but is compatible with an earlier ejection time. Additionally, the simulation shows significant cloud deceleration and disruption in just 120 yr following ejection. Together, this indicates that the bullet over-densities are likely to be higher than 10^4 , or that the ISM densities are lower than used in the models. Prior to the dynamic ejection event, the forming stars probably

produced accretion-powered outflows which would have carved cavities in the surrounding cloud through with ejecta would be moving. Additionally, some bullets may be propagating through cavities and wakes created by the leading edge of the ejected debris field.

The inclusion of cooling in the post-shock regions will tend to lower the transverse expansion of the shock-heated plasma to

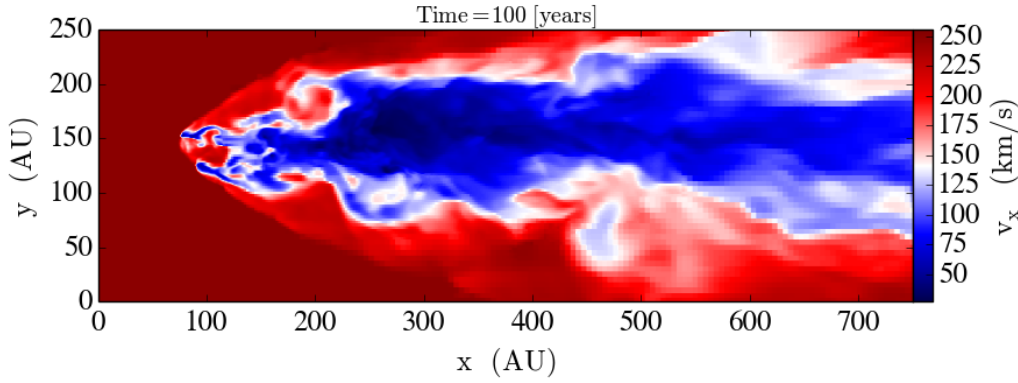


Fig. 13. Slice through the shock model showing the x -velocity from the Enzo simulation described in Sect. 3.3 at $t = 100$ yr. The velocities correspond to motions along the line-of-sight. Owing to the nature of the simulation, since the bullet is initialized at rest the medium is flowing past it, small x -velocities signify material that has not been significantly accelerated. Or, when frame-shifted to the case of a moving bullet, material that has not been significantly de-accelerated.

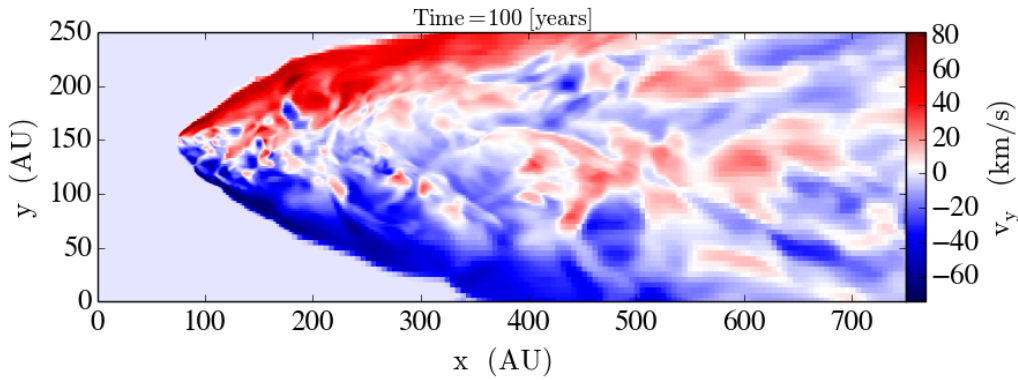


Fig. 14. Slice through the shock model showing the y -velocity from the Enzo simulation described in Sect. 3.3 at $t = 100$ yr. The velocities correspond to motions along the line-of-sight.

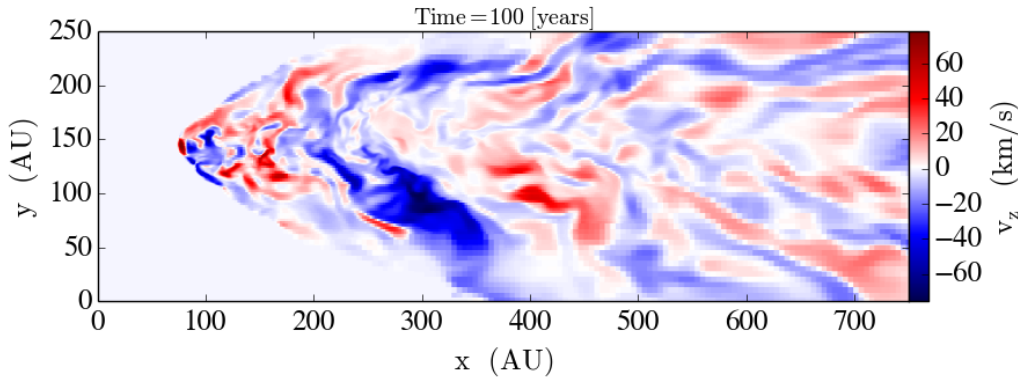


Fig. 15. Slice through the shock model showing the z -velocity from the Enzo simulation described in Sect. 3.3 at $t = 100$ yr. The velocities correspond to motions perpendicular to the motion of the bullet and the line-of-sight.

produce a narrower wake and a lower sideways splashing velocity. Cooling of the shock-heated layer produced by the slower, reverse shock moving back into the bullet will also tend to result in extensive fragmentation as portions of the cloud rapidly cool and condense – a phenomenon observed in the cloud-crushing simulations of (Silvia et al. 2010, 2012). Such fragments could have considerably longer survival times than the structures present in the simulation presented here. Other physical phenomena not included in this numerical work (e.g. magnetic fields, thermal conduction, plasma viscosity) may also aid in cloud survival. The addition of such physics is left to future work.

3.4. Other YSOs in the field

The line-of-sight to the OMC1 BN/KL outflow contains both lower-mass protostars embedded in or near the OMC1 cloud core, and more mature YSOs in the foreground Orion Nebula. Several dozen YSOs fall into the field-of-view presented here. Several of these YSOs drive outflows which can be seen in our images.

The most prominent outflow crosses the northern part of the BN/KL outflow around Declination $-05:31$ at position angle, $PA \sim 240^\circ$ to 250° and indicated by a dashed arrow near the top of Fig. 3. Comparison with the [O I] and [S II] HST images presented by Doi et al. (2002) show that this flow consists of a bow shock located at J2000 = 5:35:06.8, $-5:18:27$. Doi et al. (2002) label this feature as 115–101 and 115–102 in their Fig. 4 where it is shown as part of HH 603 and measured a proper motion toward $PA \sim 230^\circ$ with a velocity of 70 to 75 km s^{-1} . In the H_2 image, a larger but fainter bow shock is located north of 115–101 and 115–102 at J2000 = 5:35:11.6, $-5:20:54$. In our H_2 images, this $2''$ radius bow shock shows a proper motion parallel to 115–101 and 115–102 with a velocity of about 70 km s^{-1} . This feature is also faintly seen in the HST [O I] and [S II] images obtained in 1994. Assuming that the [O I], [S II], and H_2 emission arise from the same region, these images confirm the mostly west-southwest motion. Finally, the [O I] image shows a very faint bow-shaped feature at J2000 = 5:35:08.9, $-5:18:10$ with a morphology and orientation consistent with the above proper motion vectors. Apparently, this set of three west-facing and west-moving shocks traces an outflow which originates from a

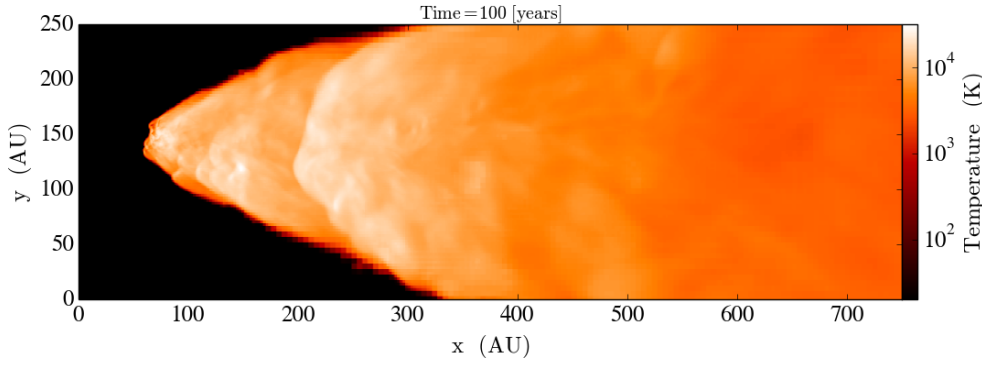


Fig. 16. Density-weighted projection of gas temperature from the Enzo simulation described in Sect. 3.3 at $t = 100$ yr. Projected values are computed such that $T_{\text{proj}} = \frac{\sum_i [T_i \times \rho_i]}{\sum_i \rho_i}$, where T_i is the projected quantity, ρ_i is the weighting quantity, and i denotes the cell number. As discussed in the text, actual post-shock temperature in slices that are not weighted by density reach temperatures in excess of 10^6 K.



Fig. 17. V2270 [Fe II] jet (blue) and H_2 emission in the region (orange).

yet-to-be identified YSO located northeast of the OMC1 core in the Integral Shaped Filament of dense gas in the Orion A cloud.

The variable star V2270 Ori (05:35:15.394, $-05:21:14.11$) located $71''$ north of BN along the line-of-sight to the eastern edge of our images drives a bipolar [Fe II] outflow at PA $\sim 34^\circ$ (Fig. 17). The flow consists of a pair of bow-shaped features $1.5''$ southwest and $2.1''$ northeast of the star. The southwest portion of the flow forms a jet extending several arc seconds beyond the southwest bow. A curved, less-collimated jet-like feature extends to the northeast. This morphology is reminiscent of a jet produced by converging flows at the end of a nozzle (Canto & Rodriguez 1980; Canto et al. 1981). Spectra were obtained at the Apache Point Observatory 3.5 m telescope using the Triplespec spectrometer (these results will be presented fully in a forthcoming paper). These spectra show that the southwestern jet is redshifted with a mean radial velocity of about $+30 \text{ km s}^{-1}$ with respect to the rest frame of the Orion Nebula [Fe II] emission. The northeast lobe of the V2270 [Fe II] jet is blueshifted with a radial velocity of about $+30 \text{ km s}^{-1}$. The velocity changes at the position of the star, indicating that V2270 Ori is the driver of this outflow.

There is a silhouette disk system at 5:35:14.692 $-5:22:20.36$ about $8''$ east of BN (Fig. 18). It is most evident in the



Fig. 18. Near-IR disk shadow located $8''$ east of BN. [Fe II] emission is shown in blue; H_2 emission is shown in orange.

[Fe II] images, but also seen in the H_2 and Ks filters. The arcsecond-scale bipolar nebula perpendicular to the shadow likely traces reflected continuum light from the central star embedded in and shadowed by the nearly edge-on disk. The shadowing occurs at position angle 9° implying a disk axis at about 99° .

4. Conclusions

New images of the OMC1 BN/KL outflow, obtained with the Gemini South MCAO laser guide star adaptive optics system are presented. The images, obtained in the $2.12 \mu\text{m}$ H_2 line, the $1.64 \mu\text{m}$ [Fe II] line, and in a broad-band K_s filter nearly reach the diffraction limit of the 8 m telescope, about $0.08''$. Complete coverage of the outflow's H_2 wakes and [Fe II] fingertips reveal over 100 individual shocks in unprecedented detail.

These images are combined with 2007 to 2009 epoch images obtained with the Gemini North AO system, Altair, and the near-IR camera NIRI, and earlier epoch natural seeing limited images to measure new proper motions of selected features and to search for morphological changes in the BN/KL outflow.

The observed morphologies of the fingers and wakes are compared with numerical hydrodynamic simulations of a compact, high density bullet moving through a lower density ambient

medium with a Mach number of about 10^3 . The main results of this investigation are:

- Several dozen [Fe II] bright fingertips and a few sub-arcsecond diameter H_2 knots show the highest proper motions. The proper motions are 150 to 300 km s^{-1} at the projected north end of the outflow complex.
- The survival of H_2 in a knot (the HVCC) moving with a proper motion or order 100 km s^{-1} indicates that it must have a density much higher than the surrounding medium. Over the last 6 yr, this feature has shown dramatic morphological changes as it approaches a high velocity [Fe II] knot located several arcseconds farther downstream. The H_2 emission from this high-velocity compact clump (HVCC) has spread laterally (orthogonal to its proper motion), expanding from a diameter less than $0.1''$ to more than $0.4''$, possibly indicating the rapid evolution of the reverse shock moving into the clump.
- Many of the wakes show measurable expansion with a velocity of up to $\sim 80 \text{ km s}^{-1}$ orthogonal to the proper motions of the fingertips which produce them. The compact structure of the [Fe II] and H_2 emission of the fingertips suggests that they are powered by sub arcsecond to arcsecond scale bullets which have a much greater density than the medium into which they are moving. It is argued that the density in the bullets must be more than three orders-of-magnitude greater than the background density.
- A simple model of bullet propagation is presented in which a fast forward shock produced mega-Kelvin plasma whose cooling length is much longer than the diameter of the bullet. The expansion of this plasma drives shocks into the medium at right angles to the bullet motion to produce $< 100 \text{ km s}^{-1}$ shocks which can sweep up the ambient medium without completely destroying H_2 . These sideways shocks driven by the expansion of the shock-heated medium are responsible for the intense H_2 emission in the OMC1 BN/KL outflow. The reverse shock moving into the bullets is slow and may excite some detectable H_2 emission.
- Preliminary numerical simulations with the Enzo code using an adiabatic equation of state reproduce the observed morphology and kinematics of the fingers. The numerical simulations reproduce the observed sideways splash, the spreading of the post-shock material orthogonal to the propagation of the bullets, and the fragmentation of the leading edge of the high-velocity debris. Further numerical modeling is needed to fine-tune the model parameters to better match the densities and dynamical ages of the observed OMC1 shocks.

Acknowledgements. This research of J.B. and A.G. was in part supported by National Science Foundation (NSF) grant AST-1009847. We thank the staff the Gemini South observatory, and in particular the contributions of F. Rigaut, B. Neichel, C. d’Orgeville, R. Carrasco, P. Michaud, and the team responsible for developing and commissioning the Gemini South Adaptive Optics Imager and the multi-conjugate adaptive optics system without which these observations would have been impossible. We thank, Richard (Deno) Stelter for assistance in the initial reduction of the Gemini North NIRI images. Many of the figures were generated with SAOImage ds9. Computing resources for the simulation were provided by the High Performance Computing Center (HPCC) at Michigan State University.

References

Allen, D. A., & Burton, M. G. 1993, *Nature*, 363, 54
 Alves, J., & Bouy, H. 2012, *A&A*, 547, A97
 Axon, D. J., & Taylor, K. 1984, *MNRAS*, 207, 241
 Bally, J., & Zinnecker, H. 2005, *AJ*, 129, 2281

Bally, J., Cunningham, N. J., Moeckel, N., et al. 2011, *ApJ*, 727, 113
 Beuther, H., & Nissen, H. D. 2008, *ApJ*, 679, L121
 Blondin, J. M., Fryxell, B. A., & Konigl, A. 1990, *ApJ*, 360, 370
 Bouy, H., Alves, J., Bertin, E., Sarro, L. M., & Barrado, D. 2014, *A&A*, 564, A29
 Bryan, G. L., Norman, M. L., O’Shea, B. W., et al. 2014, *ApJS*, 211, 19
 Canto, J., & Rodríguez, L. F. 1980, *ApJ*, 239, 982
 Canto, J., Goudis, C., Johnson, P. G., & Meaburn, J. 1980, *A&A*, 85, 128
 Canto, J., Rodríguez, L. F., Barral, J. F., & Carral, P. 1981, *ApJ*, 244, 102
 Chatterjee, S., & Tan, J. C. 2012, *ApJ*, 754, 152
 Colgan, S. W. J., Schultz, A. S. B., Kaufman, M. J., Erickson, E. F., & Hollenbach, D. J. 2007, *ApJ*, 671, 536
 Cyganowski, C. J., Whitney, B. A., Holden, E., et al. 2008, *AJ*, 136, 2391
 Doi, T., O’Dell, C. R., & Hartigan, P. 2002, *AJ*, 124, 445
 Doi, T., O’Dell, C. R., & Hartigan, P. 2004, *AJ*, 127, 3456
 d’Orgeville, C., Diggs, S., Fesquet, V., et al. 2012, in *SPIE Conf. Ser.*, 8447
 Draine, B. T. 2011, *Physics of the Interstellar and Intergalactic Medium* (Princeton University Press)
 Eislöffel, J. 2000, *A&A*, 354, 236
 Fesen, R. A., Zastrow, J. A., Hammell, M. C., Shull, J. M., & Silvia, D. W. 2011, *ApJ*, 736, 109
 Furuya, R. S., & Shinnaga, H. 2009, *ApJ*, 703, 1198
 Genzel, R., Reid, M. J., Moran, J. M., & Downes, D. 1981, *ApJ*, 244, 884
 Gies, D. R., & Bolton, C. T. 1986, *ApJS*, 61, 419
 Goddi, C., Humphreys, E. M. L., Greenhill, L. J., Chandler, C. J., & Matthews, L. D. 2011, *ApJ*, 728, 15
 Gómez, L., Rodríguez, L. F., Loinard, L., et al. 2005, *ApJ*, 635, 1166
 Gómez, L., Rodríguez, L. F., Loinard, L., et al. 2008, *ApJ*, 685, 333
 Graham, M. F., Meaburn, J., & Redman, M. P. 2003, *MNRAS*, 343, 419
 Greenhill, L. J., Gwinn, C. R., Schwartz, C., Moran, J. M., & Diamond, P. J. 1998, *Nature*, 396, 650
 Grosso, N., Feigelson, E. D., Getman, K. V., et al. 2006, *A&A*, 448, L29
 Gualandris, A., Portegies Zwart, S., & Eggleton, P. P. 2004, *MNRAS*, 350, 615
 Gull, T. R., Goad, L., Chiu, H.-Y., Maran, S. P., & Hobbs, R. W. 1973, *PASP*, 85, 526
 Hoogerwerf, R., de Bruijne, J. H. J., & de Zeeuw, P. T. 2000, *ApJ*, 544, L133
 Hoogerwerf, R., de Bruijne, J. H. J., & de Zeeuw, P. T. 2001, *A&A*, 365, 49
 Jones, B. F., & Walker, M. F. 1985, *AJ*, 90, 1320
 Kaifu, N., Usuda, T., Hayashi, S. S., et al. 2000, *PASJ*, 52, 1
 Kwan, J., & Scoville, N. 1976, *ApJ*, 210, L39
 Lee, J.-K., & Burton, M. G. 2000, *MNRAS*, 315, 11
 McCaughrean, M. J., & Mac Low, M.-M. 1997, *AJ*, 113, 391
 Menten, K. M., Reid, M. J., Forbrich, J., & Brunthaler, A. 2007, *A&A*, 474, 515
 Milisavljevic, D., & Fesen, R. A. 2013, *ApJ*, 772, 134
 Muench, A. A., Lada, E. A., Lada, C. J., & Alves, J. 2002, *ApJ*, 573, 366
 Münch, G., & Taylor, K. 1974, *ApJ*, 192, L93
 Neichel, B., D’Orgeville, C., Callingham, J., et al. 2013, *Proc. Third AO4ELT Conf.*, eds. S. Esposito, & L. Fini
 Neichel, B., Rigaut, F., Vidal, F., et al. 2014, *MNRAS*, 440, 1002
 Nissen, H. D., Gustafsson, M., Lemaire, J. L., et al. 2007, *A&A*, 466, 949
 Perets, H. B., & Šubr, L. 2012, *ApJ*, 751, 133
 Plambeck, R. L., Wright, M. C. H., Friedel, D. N., et al. 2009, *ApJ*, 704, L25
 Poveda, A., Ruiz, J., & Allen, C. 1967, *Boletín de los Observatorios Tonantzintla y Tacubaya*, 4, 86
 Reipurth, B., & Bally, J. 2001, *ARA&A*, 39, 403
 Reipurth, B., & Mikkola, S. 2012, *Nature*, 492, 221
 Reipurth, B., Mikkola, S., Connolly, M., & Valtonen, M. 2010, *ApJ*, 725, L56
 Rigaut, F., Neichel, B., Boccas, M., et al. 2012, in *SPIE Conf. Ser.*, 8447
 Rigaut, F., Neichel, B., Boccas, M., et al. 2014, *MNRAS*, 437, 2361
 Rodríguez, L. F., Poveda, A., Lizano, S., & Allen, C. 2005, *ApJ*, 627, L65
 Sahai, R., Claussen, M., Sánchez Contreras, C., Morris, M., & Sarkar, G. 2008, *ApJ*, 680, 483
 Silvia, D. W., Smith, B. D., & Shull, J. M. 2010, *ApJ*, 715, 1575
 Silvia, D. W., Smith, B. D., & Shull, J. M. 2012, *ApJ*, 748, 12
 Smith, M. D., & Rosen, A. 2007, *MNRAS*, 378, 691
 Smith, N., Whitney, B. A., Conti, P. S., de Pree, C. G., & Jackson, J. M. 2009, *MNRAS*, 399, 952
 Snell, R. L., Scoville, N. Z., Sanders, D. B., & Erickson, N. R. 1984, *ApJ*, 284, 176
 Stone, J. M., Xu, J., & Mundy, L. G. 1995, *Nature*, 377, 315
 Tan, J. C. 2004, *ApJ*, 607, L47
 Turk, M. J., Smith, B. D., Oishi, J. S., et al. 2011, *ApJS*, 192, 9
 Wiseman, J. J., & Ho, P. T. P. 1996, *Nature*, 382, 139
 Wu, Y., Liu, T., & Qin, S.-L. 2014, *ApJ*, 791, 123
 Zapata, L. A., Schmid-Burgk, J., Ho, P. T. P., Rodríguez, L. F., & Menten, K. M. 2009, *ApJ*, 704, L45
 Zapata, L. A., Schmid-Burgk, J., Pérez-Goytia, N., et al. 2013, *ApJ*, 765, L29